


Land Use/Land Cover (LULC) classification based on SAR/Sentinel 1 image in Distrito Federal, Brazil

*Felipe Lima Ramos Barbosa*¹ 

*Renato Fontes Guimarães*² 

*Osmar Abílio de Carvalho Júnior*³ 

*Roberto Arnaldo Trancoso Gomes*⁴ 

Keywords:

SAR
Sentinel 1
interferometric coherence
urban environment
urban objects

Abstract

The social and environmental challenges are directly related to the existing population concentration in urban environments, contributing to more than 75% of the world's Gross Domestic Product (GDP). Thus, the Land Use and Land Cover (LULC) dynamics are essential to support public policy elaboration and implementation. SAR systems, especially the interferometry techniques, have shown remarkable results in this challenge since they do not have direct influence from the atmosphere. Few studies used interferometric coherence from the Sentinel-1 image in an urban environment. This research aims to classify the LULC in the Distrito Federal, Brazil, based on different dimensions considering the intensity and interferometric coherence for the year 2018. The results measured from the Kappa and F1 metrics indicate that the insertion of a time series of interferometric coherencies improves the performance of the classification, from 0.50 to 0.75 (Kappa) and from 0.54 to 0.79 (F1), a fact that was evident in the improved performance of the thematic classes related to vegetation cover. Furthermore, the best identification of urban objects used only the intensities (VV and VH) in the classification.

¹ Universidade de Brasília, Departamento de Geografia, Brasília, DF, Brazil. felipelrb@gmail.com

² Universidade de Brasília, Departamento de Geografia, LSIE, Brasília, DF, Brazil. renatofg@unb.br

³ Universidade de Brasília, Departamento de Geografia, LSIE, Brasília, DF, Brazil. osmarjr@unb.br

⁴ Universidade de Brasília, Departamento de Geografia, LSIE, Brasília, DF, Brazil. robertogomes@unb.br

INTRODUCTION

The concentration of population in Brazilian cities is responsible for a significant part of the social and environmental problems, since approximately 160 million people live in the urban environment, about 85% of the population, as said by 2010 Demographic Census prepared by the Instituto Brasileiro de Geografia e Estatística (IBGE). According to [Zhu et al. \(2019\)](#), urban areas guarantee more than 75% of the world's Gross Domestic Product (GDP).

Land Use/ Land Cover (LULC) information is indispensable for public environmental policies ([KHALIL; HAQUE, 2018](#)). The LULC dynamic is one of the most expressive areas in remote sensing, being a key element in the environmental impact assessment, ecological monitoring, global change monitoring, territorial planning, development of regulatory policies, and identification and prevention of irregular urban expansion.

Synthetic Aperture Radar (SAR) image has the advantage of being nearly free of atmospheric interference and cloud cover, facilitating the analysis of changes over time. SAR data has improved and popularized the development of studies focused on LULC classification ([DINIZ; GAMA, 2019](#); [MIGUEL; SANO, 2019](#)), optical and radar data fusion ([RAJAH et al., 2018](#); [WERNER et al., 2014](#)), oil spills ([CHATURVEDI et al., 2019](#); [OZIGIS et al., 2020](#)), mass gravitational movements ([AUBLANC et al., 2018](#); [LI et al., 2020](#)) and agricultural mapping ([PICHIERRI et al., 2018](#); [SEKERTEKIN et al., 2020](#)).

SAR systems also have the potential for identifying urban objects. The radiation control emitted and received by the sensor allows a better understanding of the structures and geometric objects on the ground, as their dielectric properties affect electromagnetic radiation's polarization ([WERNER et al., 2014](#)). However, the SAR system presents some factors that interfere with the quality of imaging of natural and artificial surfaces due to abrupt changes in height, orientation, shape, and size of objects, which together promote a spectral confusion between the LULC classes to be mapped ([GRIFFITHS et al., 2010](#)).

The use of the interferometric technique (InSAR) allows the enhancement of LULC classifications. The wave phase (Φ) in the SAR signal represents the electromagnetic wave's return moment and is related to the distance

between the satellite antenna and the targets. Therefore, it can be used as information on the derivation of distortions in the terrain (mass movements, undercuts, Digital Terrain Models, and others). The wave phase (Φ) calculation considers the following mathematical equation (Equation 1), whereas the sinusoidal nature respects a circle of 2π .

$$\Phi = \frac{2\pi}{\lambda} 2R = \frac{4\pi}{\lambda} Rv \tag{1}$$

This technique measures the difference between the phases of two SAR scenes from the same area and obtained at different incident angles, which defines the phase change, or interferometric phase ($\Delta\Phi$). Hypothetical geometry of an InSAR system obtained from two orbits apart by an interferometric baseline (Figure 1).

Figure 1. InSAR geometry scheme obtained from two orbits

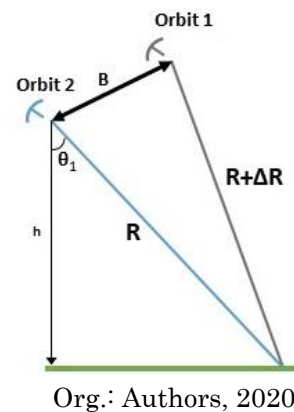


Figure 1 shows the measurements directly relate to the distance covered by the signal, the interferometric baseline, the viewing angles, and the wavelength (λ). Equations 2 and 3 describe the geometric interface of the interferogram concept.

$$\Phi_1 = \frac{4\pi R}{\lambda}, \Phi_2 = \frac{4\pi(R + \Delta R)}{\lambda} \tag{2}$$

$$\Delta\Phi = \Phi_2 - \Phi_1 = \frac{4\pi\Delta R}{\lambda} \tag{3}$$

InSAR techniques provide helpful information to support urban environment studies, mainly focused on identifying subsidence movements through surface deformation analysis ([CIAMPALINI et al., 2019](#); [HU et al., 2019](#)). Hence, it is essential to

ensure a good quality of both return signals to perform interferometric analysis.

Coherence (γ) is an ancillary interferometric measurement that ranges from 0 to 1 and indicates the degree of similarity of the phases of both return signals in an InSAR system. This metric indicates the areas that may be subject to interferometric studies, a direct result of the combination of a specific geometric pattern of the system and the environmental conditions during the registration of both signals. Equation 4 defines the interferometric coherence between two SAR images, resulting from the relation between the real and expected values of the amplitudes $|u_1|$ and $|u_2|$ of the two original SAR images.

$$\gamma = \frac{E[u_1 u_2]}{\sqrt{E[|u_1|^2]} \cdot \sqrt{E[|u_2|^2]}} \quad (4)$$

Interferometric coherence is valuable supplementary information for landscape classification (OLESK et al., 2016; WEGMULLER et al., 2015), once its values are associated with temporal, geometric, volumetric, and signal processing characteristics. Studies use coherence in the vegetation cover identification (DINIZ; GAMA, 2019; MOHAMMADIMANESH et al., 2018), due to its volumetric behavior in time series. Such areas are quite heterogeneous and show high texture changes over time, caused by different weather conditions or LULC conversion. The coherence variation caused by the temporal correlation helps identify different spectro-temporal curves of targets and serves as ancillary information for their classification.

Coherence has a high potential for urban mapping (MIGUEL; SANO, 2019; SICA et al., 2019; ZHANG et al., 2018). Urban objects

(buildings, houses, walls) do not have great backscatter values variation regarding a time series, which leads to the registration of high coherence rates over such areas. Further, few studies use interferometric coherence from the Sentinel-1 satellite in urban environments (KHALIL; HAQUE, 2018).

This study aims to classify LULC in part of the Distrito Federal (DF) using a SAR time series from the Sentinel-1 image for the year 2018. For this purpose, we tested different temporal arrangements considering the intensity (dB) and interferometric coherence in the image classification.

AREA OF STUDY

Distrito Federal (DF) has a population of approximately 3,000,000 inhabitants with asymmetrical distribution between rural (3.38%) and urban (96.62%), as shown in its Ecological-Economic Zoning (BRASIL, 2018). The DF urban environment has several arrangements that mostly materialize in its planned part, with buildings and residences arranged in wooded areas, or unplanned, which tends to behave as typical urban arrangements found in other Brazilian cities. Figure 2 illustrates different urban object arrangements in the DF.

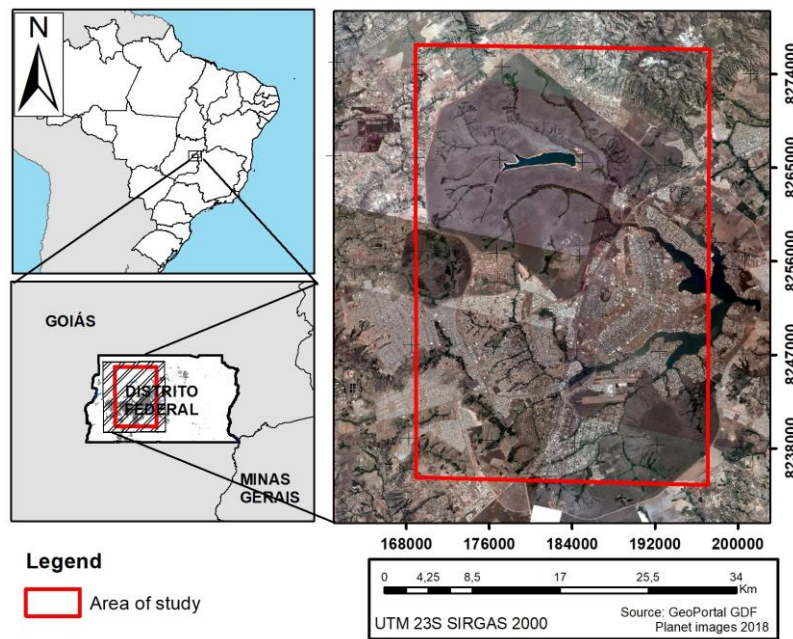
The study area comprises the perimeter established between the coordinates 48°5'57.31 "W 15°34'23.04" S and 47°49'50.10 "W 15°57'8.3" S (Figure 3). This area's choice is due to (i) diversification of the urban morphology and Cerrado vegetation types; and (ii) limited computational capacity in the SAR processing for the entire year of 2018, mainly interferometric data.

Figure 2. Several urban arrangements in the DF. (a) Planned and largely wooded area; (b) Planned and less wooded area; (c) Recent unplanned expansion area.



Org.: Authors, 2020

Figure 3. Area of study relative to the part of the DF.



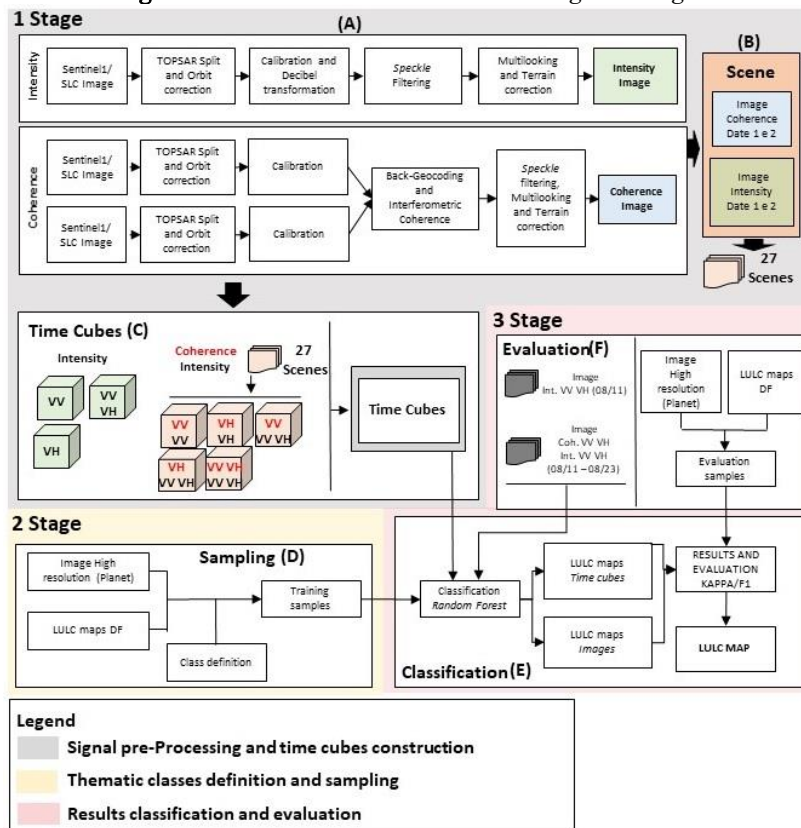
Org.: Authors, 2020

MATERIALS AND METHODS

We organized the methodology into three stages (Figure 4). The first stage refers to the

pre-processing of radar signals and the construction of time cubes. The second stage concerns the class definition and the choice of training samples. The third stage deals with the classification and evaluation procedures.

Figure 4. Flowchart of the methodological stages



Org.: Authors, 2020

Radar signal pre-processing and time cubes construction (Stage 1)

Sentinel 1, an initiative of the European Commission and European Space Agency (ESA), is a constellation of two orbital platforms operating in the C band (5,405 GHz) of the microwave, in two polarizations (VV and VH), and has 4 (four) acquisition modes: (i) Stripmap (SM); (ii) Interferometric Wide Swath (IW); (iii) Extra-Wide Swath (EW); and (iv) Wave mode (WV). We chose the IW acquisition mode, with a 250-km imaging range, moderate resolution (5m by 20m), and structured in Terrain Observation with Progressive Scans

SAR (TOPSAR), which ensures homogeneous image quality (DE ZAN; GUARNIERI, 2006). The LULC mapping widely uses the IW acquisition mode.

Sentinel 1 images can be acquired at different levels of processing: (i) Single Look Complex (SLC); and (ii) Ground Range Detected (GRD). Considering the interferometric application, we selected SLC images for the year 2018 since they have information related to amplitude and signal phase, recorded in complex numbers, and projected in slant-range. Table 1 shows the dates of the 28 Sentinel 1 IW/SLC images acquired.

Table 1. Dates of Sentinel 1 images acquired and processed

Dates – Sentinel 1 images (IW SLC)			
01/07/2018	04/01/2018	07/18/2018	10/10/2018
01/19/2018	04/13/2018	07/30/2018	10/22/2018
01/31/2018	04/25/2018	08/11/2018	11/03/2018
02/12/2018	05/07/2018	08/23/2018	11/15/2018
02/24/2018	05/19/2018	09/04/2018	11/27/2018
03/08/2018	06/12/2018	09/16/2018	12/09/2018
03/20/2018	06/24/2018	09/28/2018	12/21/2018

Org.: Authors, 2020.

The pre-processing (Figure 4A) reduces radiometric and geometric distortions. We use the SNAP program, developed by the European Space Agency (ESA), which has specific tools for processing the intensity and interferometric coherence from the Sentinel-1 image. We clipped the SAR images from the study area and corrected them, considering their complementary information to the satellite's orbit and altitude. In the case of intensity values estimation, we calibrate the signal to perform the transformation of the backscatter values, initially in digital levels (ND) to sigma (σ) and later transformed in decibel levels (dB), which guarantees a better representation of the values in the available range of the image histogram.

We perform a convolutional median filtering (5x5 window size) to reduce the speckle effect. This effect causes differentiation in the backscatter values that may not be associated with real landscape changes, causing a "salt and pepper" granulated pattern. Later, we transformed the SAR images, originally projected in slant-range, into a regular ground grid, a process known as multilooking.

Finally, we orthorectified and projected the SAR images in UTM 23S, WGS 1984 datum, concerning the Shuttle Radar Topography Mission (SRTM) Digital Elevation Model (30-meters resolution), which resulted in final SAR images with 10-meters resolution. These geometric corrections reduce the distortions associated with foreshortening, layover, and shadowing.

The coherence calibration of the SAR signal, designed to maintain the amplitude and phase information, kept the values adjusted in complex numbers. As an InSAR system with Sentinel 1 images can only be structured in a monostatic approach, in which the simulation of the interferometric baseline is obtained by acquiring two scenes of different times over the same area, we group the images in pairs considering the ancillary orbit information through the back-geocoding process, in order to georeference the amplitude and phase and, thus, allow the computation of the interferometric coherence according to Equation 4. The 27 interferometric coherence images calculated for the year 2018 (Box 1).

Box 1. Adopted arrangement for the 2018 interferometric coherence estimation.

Date	Coh.	Date	Coh.	Date	Coh.	Date	Coh.
01/07/2018	1	04/01/2018	8	07/18/2018	15	10/10/2018	22
01/19/2018		04/13/2018		07/30/2018		10/22/2018	
01/19/2018	2	04/13/2018	9	07/30/2018	16	10/22/2018	23
01/31/2018		04/25/2018		08/11/2018		11/03/2018	
01/31/2018	3	04/25/2018	10	08/11/2018	17	11/03/2018	24
02/12/2018		05/07/2018		08/23/2018		11/15/2018	
02/12/2018	4	05/07/2018	11	08/23/2018	18	11/15/2018	25
02/24/2018		05/19/2018		09/04/2018		11/27/2018	
02/24/2018	5	05/19/2018	12	09/04/2018	19	11/27/2018	26
03/08/2018		06/12/2018		09/16/2018		12/09/2018	
03/08/2018	6	06/12/2018	13	09/16/2018	20	12/09/2018	27
03/20/2018		06/24/2018		09/28/2018		12/21/2018	
03/20/2018	7	06/24/2018	14	09/28/2018	21		
04/01/2018		07/18/2018		10/10/2018			

Org.: Authors, 2020

In the interferometric coefficients, we applied the same filtering, multilooking, and terrain geometric correction. The interferometric coherence values in the slant-range projection used the original signal phase information in complex numbers for each image pair to be compatible with the intensity metrics. The interferometric coherence images also have a 10-meter resolution. We process all SAR information in SIRGAS 2000, according to Resolution IBGE 01/2015 (BRASIL, 2015).

After preprocessing the SAR information, we combine the 2018 intensity images into different matrix structures containing all the interstice analyzed information (time cubes) (Figure 4C). This matrix arrangement is specific for the spectro-temporal analysis within the Abilius program, which can quantitatively analyze a target considering its temporal variability.

We have structured different time cubes by initially combining only the intensity metrics in both polarizations, to evaluate the polarization performances in the classification. Besides, in order to make the interferometric coherencies and intensities compatible in the same matrix structure, it was necessary to establish 27 distinct scenes, each one with (i) coherence image and (ii) the average value of the intensities relative to the dates of the images that formed the respective interferometric pair (Figure 4B), which were finally grouped observing the temporal arrangements already mentioned (Box 1).

It was possible to structure 3 different time cubes using only the intensity measures, and

another 5 different time cubes considering the possible combinations between the interferometric coherence and intensities, in their different polarizations (Figure 4C). This methodological arrangement allowed the acquisition of 8 LULC classifications for the 2018 time series.

Training classes and samples definition (Stage 2)

The research used seven LULC classes: (i) water; (ii) grassland formation; (iii) savanna formation; (iv) forest formation; (v) flat areas, (vi) urban sprawl, and (vii) buildings (Figure 4D). LULC maps commonly use the first four classes. The "flat area" class registers the locations with lower intensity values, such as roads, parking lots, and exposed soil. This class was crucial to avoid possible confusion with water since the backscatter signal's responses are very similar due to the dominant specular effect.

In this research, the urban theme has two focuses: (i) the area identification containing the aggregate of urban objects (buildings and constructions) and green areas; and (ii) urban object identification. The urban areas have double or triple backscatter of the signal due to their interaction with objects with flat and orthogonal surfaces inherent to building facades, called the double-bounce effect, which facilitates the identification of such targets. For the first approach training, we defined the "urban sprawl" class considering different arrangements regarding the orientation and

concentration of urban objects and the surrounding green areas (Figure 2). This transition class between urban objects and the other LULC classes is because the term "urban" does not have a single meaning and makes it impossible to define different physical structures and surface properties. The second approach consisted of training samples related to the urban objects mapped through the cadastral air survey of the DF carried out in 2016.

We established 20 regions of interest for each thematic class, representing a sample cluster of approximately 6,400 pixels. This strategy aimed to maintain the stratiform distribution among the samples in each of the classification processes. The sampling process used: (i) photointerpretation of 2018 high-resolution Planet images; (ii) vegetation maps of the DF elaborated by the local government in the context of the Ecological-Economic Zoning of the DF (BRASIL, 2018); and (iii) LULC map elaborated in 2019 by the local government.

The exception was the "building" class, which we trained with the random selection of 100 buildings, with more than 500 m² each, originated from the urban cadastral air survey held in 2016. These quantities ensure the same sample cluster value as the other thematic training classes. We use the ENVI 4.3 program to perform the processing of this stage.

Classification process stage (Stage 3 E)

The Random Forest (RF) algorithm (BREIMAN, 2001) makes predictions from a set of decision trees created randomly with the relevant information. For each k th tree of the set to be composed by the algorithm, a random vector \mathcal{O}_k is generated, independent of past random vectors $\mathcal{O}_1, \dots, \mathcal{O}_{k-1}$, but with the same distribution. Hence, a tree is structured using the training samples and \mathcal{O}_k , resulting in the definition of the classifier $h(x, \mathcal{O}_k)$. Each k th tree's nodes are defined based on the nature data in a random pattern, always ensuring the best entropy between a node and its subsequent (BELGIU; DRAGUT, 2016; BREIMAN, 2001; WHITCOMB et al., 2009). Each random classifier votes, establishing the highest probability of occurrence.

We chose this classifier because of the sample size since the most robust algorithm in this situation is associated with the set of decision trees (MAXWELL et al., 2018). Miguel and Sano (2019) and Lawrence and Moran (2015) found satisfactory results regarding RF's

potential compared to other machine learning algorithms.

The Spatial Information System Laboratory (LSIE) of the Universidade de Brasília (UnB) develops the free program Abilius that has tools for visualization, digital image processing, and machine learning classification. The Abilius software structures the images in temporal cubes, allowing an efficient and rapid quantitative analysis of the spectral-temporal dynamics.

The RF algorithm implemented in Abilius comes from the Open Source Vision Library (OpenCV), using the parameterization according to Prinzie and Van den Poel (2008). We chose in 5 the maximum number of division of the decision trees and in 500, the maximum number of the set of trees (MAXWELL et al., 2018). Several academic papers used this algorithm for the classification of agricultural commodities (BITENCOURT, 2020; COSTA, 2020), land use/land cover (MARQUES et al., 2019; SALGADO, 2019), flooded areas (FERREIRA, 2018), and burned areas (OLIVEIRA, 2019).

Evaluation of classifications (Stage 3 F)

The accuracy analysis used an independent truth dataset to calculate the following metrics widely used in remote sensing studies: (i) Kappa index, and (ii) F1 score (CAO et al., 2020; SALGADO et al., 2019). The Kappa index and the F1 score come from the confusion matrix, counting true positives (TP), false positives (FP), true negatives (TN), and false negatives (FN). The calculation of the F1 score (Equation 5) considers precision (Equation 6) and recovery (Equation 7).

$$Precision = \frac{\Sigma \text{True positives (TP)}}{\Sigma \text{True positives (TP)} + \Sigma \text{False positives (FP)}} \quad (5)$$

$$Recall = \frac{\Sigma \text{True positives (TP)}}{\Sigma \text{True positives (TP)} + \Sigma \text{False negatives (FN)}} \quad (6)$$

$$F1 = 2 * \frac{Precision * Recall}{Precision + Recall} \quad (7)$$

A high precision value and a low recall value indicate inadequately mapping for a given class, even if many of these are correct compared to the "truth". Meanwhile, high recall and low precision values indicate that the class was overestimated in the study area, containing many commission errors. For each of the seven classes, we have established 300 random "truth" points independent of the training samples (BITENCOURT, 2020;

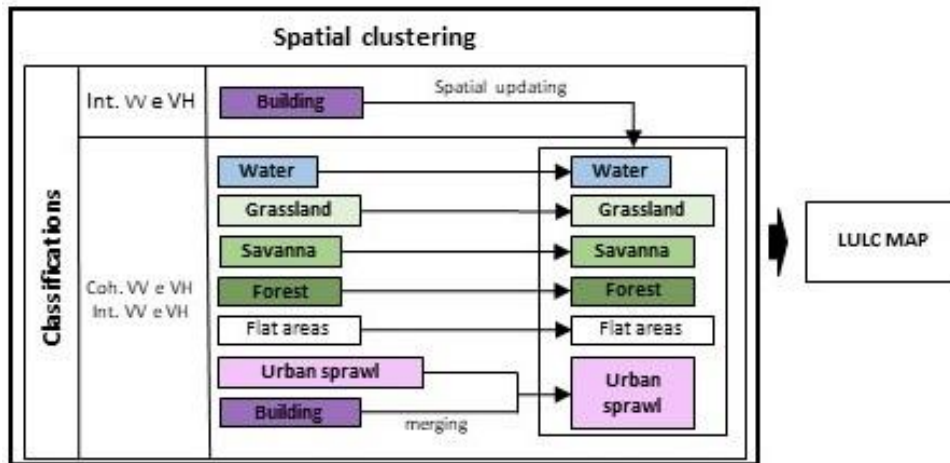
COSTA, 2020). For the definition of these random points, we used the same list of cartographic products presented in step 2.

In the time-series analysis, we compare the classifications made with two dataset (Figure 4F): (a) only the intensities in the VV and VH polarizations of 08/11/2018, and (b) interferometric coherences and the intensities, in both polarizations, referring to 08/11/2018 and 08/23/2018.

Consolidation of LULC map (Stage 3 E)

The LULC map results from the classes' spatial grouping considering their best classifications. The final map's spatial clustering considers the building class from the VV and VH intensity as the better accuracy, with its result superimposed on the best performance classification achieved (Figure 5).

Figure 5. Flowchart of LULC map consolidation



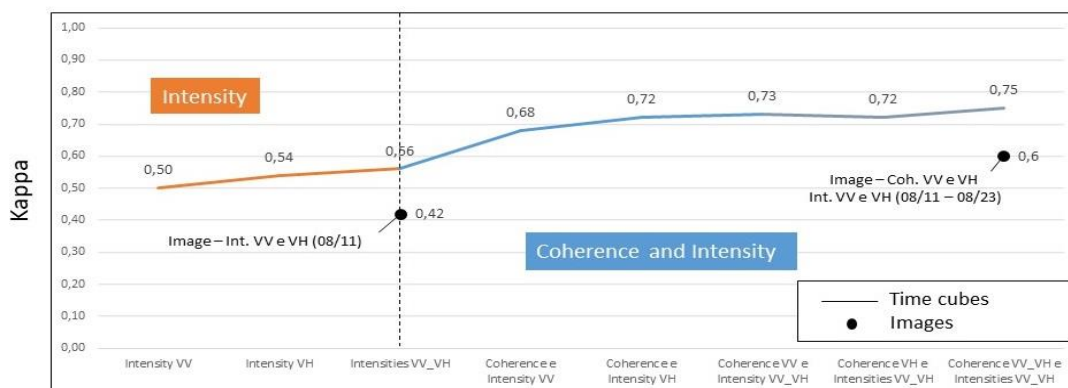
Org.: Authors, 2020

RESULTS AND DISCUSSION

This section presents the results and discussions of the eight different temporal classifications. Figures 6 and 7 show respectively the Kappa coefficient and F1-score, considering (i) only the intensities (VV and VH) (brown colour), (ii) the conjugation with the interferometric coherence (blue colour), and (iii) image classifications of 08/11 and 08/23. The time-series data produces a considerable

classification improvement, with an increase of Kappa from 0.42 to 0.56 and F1-score from 0.49 to 0.59 using only VV and VH intensities. The classification in conjunction with interferometric coherence increased the Kappa from 0.6 to 0.75 and the F1-score from 0.65 to 0.79. The temporal cube combining coherence and intensities in both polarizations achieved the best performance with 0.75 (Kappa) and 0.79 (F1-score). Moreover, the results also indicate better performances of the temporal classifications than a single period.

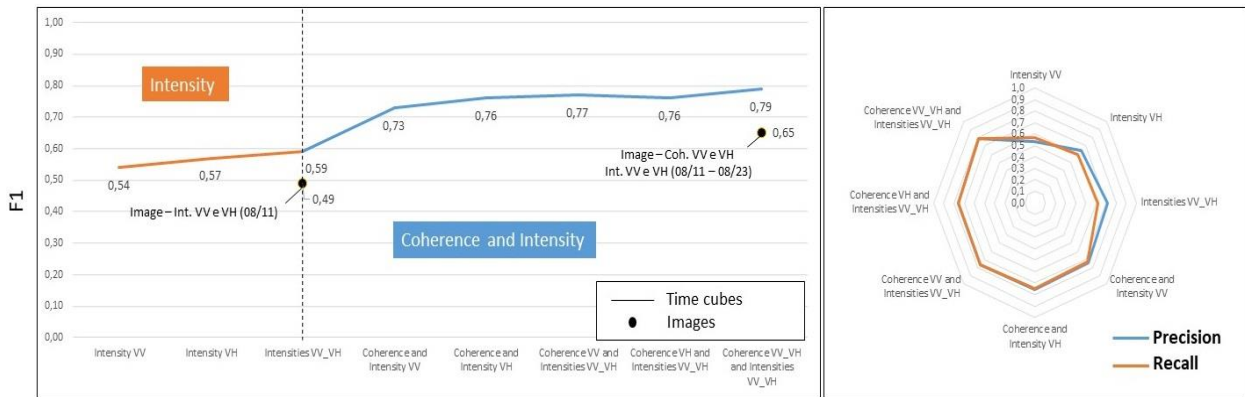
Figure 6. Performance of classifications based on the Kappa index



Classifications – Time cubes

Org.: Authors, 2020

Figure 7. Performance of classifications based on F1 score, precision and recall.



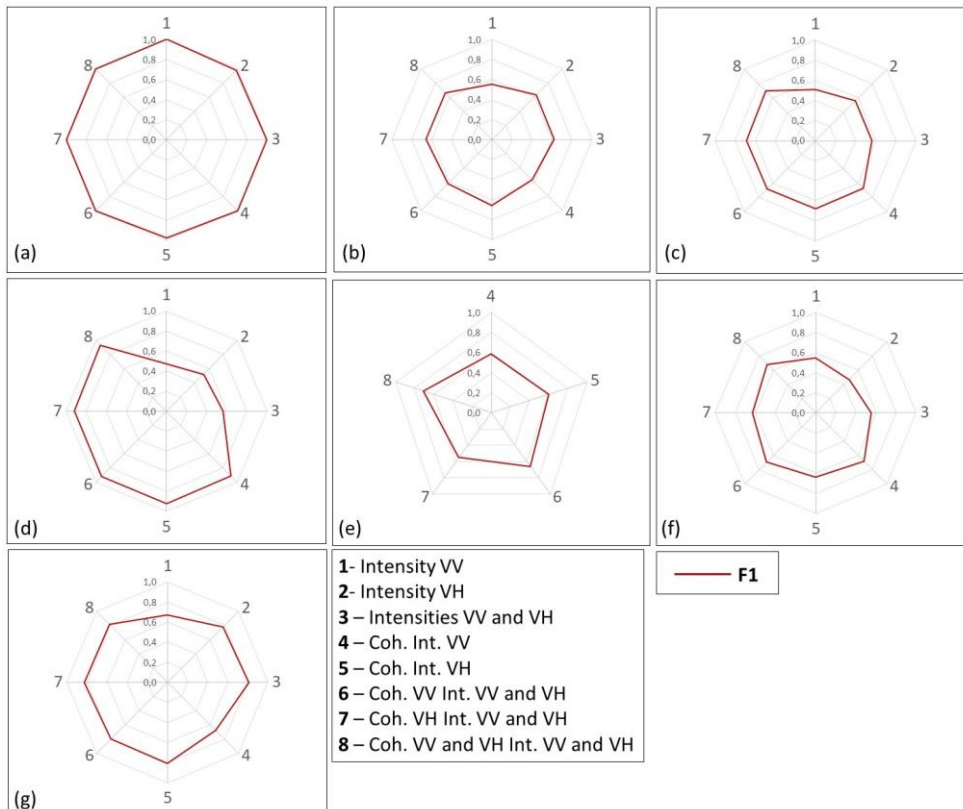
Classifications – Time cubes

Org.: Authors, 2020.

The F1-score for each class shows different responses regarding interferometric coherence in the classification (Figure 8). Figure 9 presents the precision and recall metrics for each class. Classification 8, which considers the

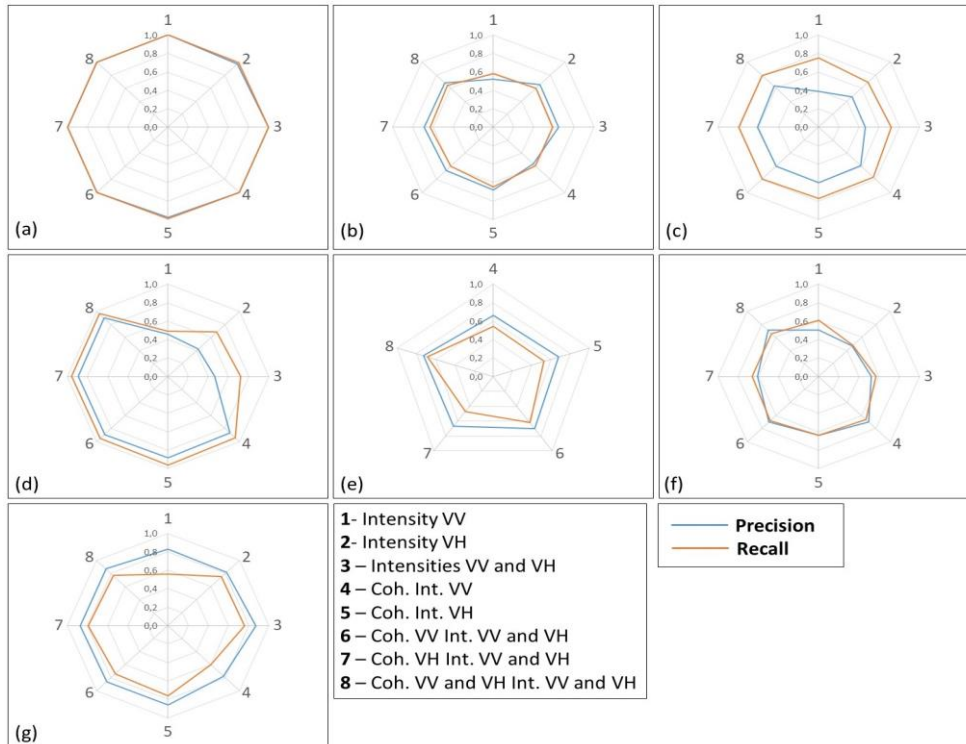
VV and VH intensities and interferometric coherence, reaches the best F1, i.e., the best balance of precision and recall values (Figure 9).

Figure 8. Performance of the classifications by thematic class based on the F1 index - (a) Water; (b) Grassland formation; (c) Savanna formation; (d) Forest formation; (e) Urban sprawl; (f) Building and (g) Flat areas.



Org.: Authors, 2020

Figure 9. Performance of the classifications by thematic class - precision and recall indexes - (a) Water; (b) Grassland formation; (c) Savanna formation; (d) Forest formation; (e) Urban sprawl; (f) Building and (g) Flat areas.



Org.: Authors, 2020

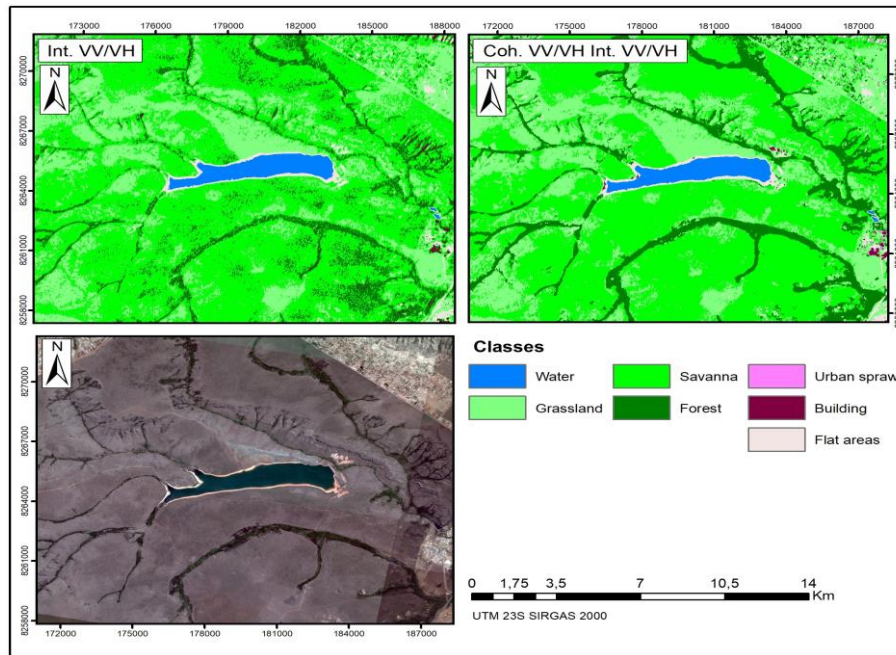
The F1-score reveals significant performance changes in the vegetation classes, specifically savanna and forest formation (Figure 8c and 8d). The results indicate an increase from 0.51 to 0.70 (savanna) and from 0.47 to 0.93 (forest) when considering the interferometric coherence in the classification, in this case, assuming all possible polarization combinations. The savanna class showed little variation in the recall values and a significant improvement in the precision values (0.39 to 0.63), which indicates a decrease in FP (Figure 9c). In the forest class, the performance improvement becomes more noticeable, in which both precision and recall metrics increased from 0.46 to 0.90 and from 0.49 to 0.96, respectively (Figure 9d). These results demonstrate a significant decrease in FN and

FP, thus providing a more reliable model for identifying vegetative classes, especially those with less temporal variation in forest density. Figure 10 shows the improvement in the vegetation classification with the interferometric coherence time series.

Urban objects versus Urban sprawl (Stage 3 E)

The urban classes showed different results with the use of coherence in the classification. The urban sprawl class only became evident with coherence images. Figure 8e shows an increase of F1-score from 0.59 to 0.71 using intensities and consistencies in both polarizations in the classification and a better balance between precision and recall values (Figure 9e).

Figure 10. Performance of vegetation cover classes.

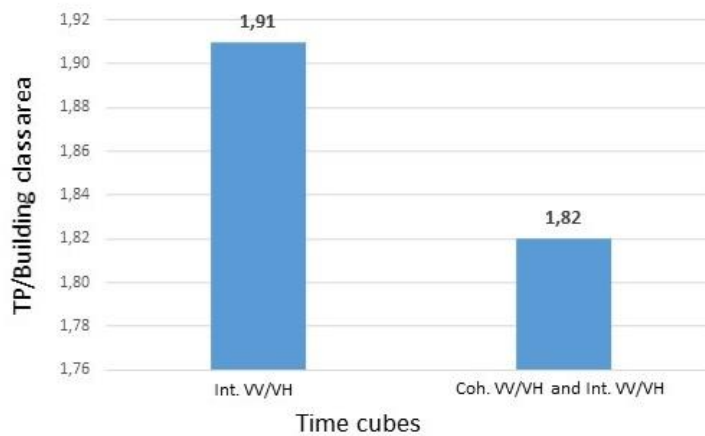


Org.: Authors, 2020.

The building class increases F1-score from 0.55 to 0.68 (Figure 8f). It is noticeable that the increases in precision (0.50 to 0.71) and recall (0.48 to 0.66) values (Figure 9f) are associated with the mapping of a more generic class in the study area, which does not necessarily indicate a better definition of urban

objects. Figure 11 shows the TP values for the building class divided by the areas that were classified considering the results (i) using only the intensities (VV and VH) and (ii) the aggregate of interferometric coherencies and intensities in both polarizations.

Figure 11. TP values divided by buildings class areas



Org.: Authors, 2020

The index indicates that the respective building class is higher in the time series using only the intensities than the whole data dimensionality (Figure 11), which appears to be adequate in the area with a predominant double bounce effect. Despite having better accuracy rates, the interferometric coherence tends to potentiate the result of the building

class overestimating its area in the LULC classification.

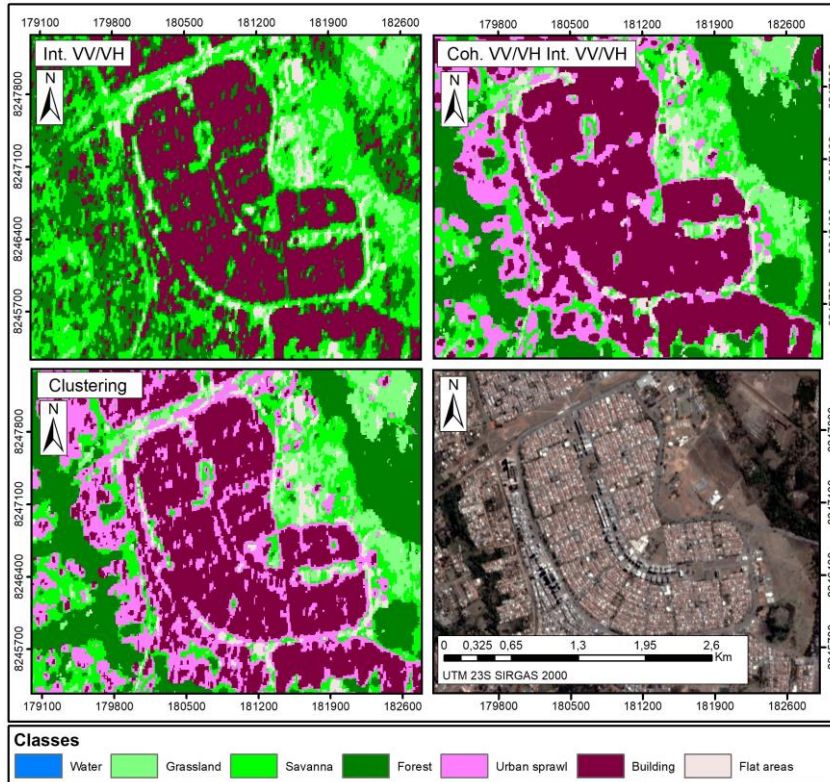
Compilation of the LULC map

The final LULC map grouped the classifications with the best performance with the Kappa coefficient and F1 score. The exception was the building class, which

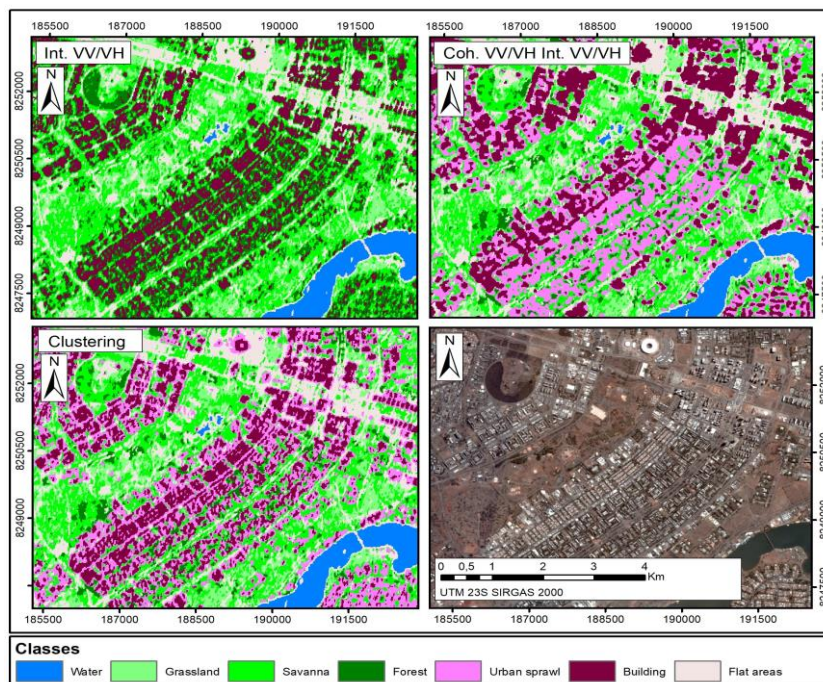
considered the classification using only the VV and VH intensities. Figure 12 presents two regions of the study area to exemplify the refinement carried out by the process of spatial clustering of the best thematic performances defined.

The proposed method of LULC map compilation provided a most reliable registration of urban objects in the final classification result, regions characterized by a double bounce effect. Figure 13 shows the LULC map from the proposed methodology.

Figure 12. Examples of refinement of the urban theme - regions of (a) Guara and (b) Plano Piloto.



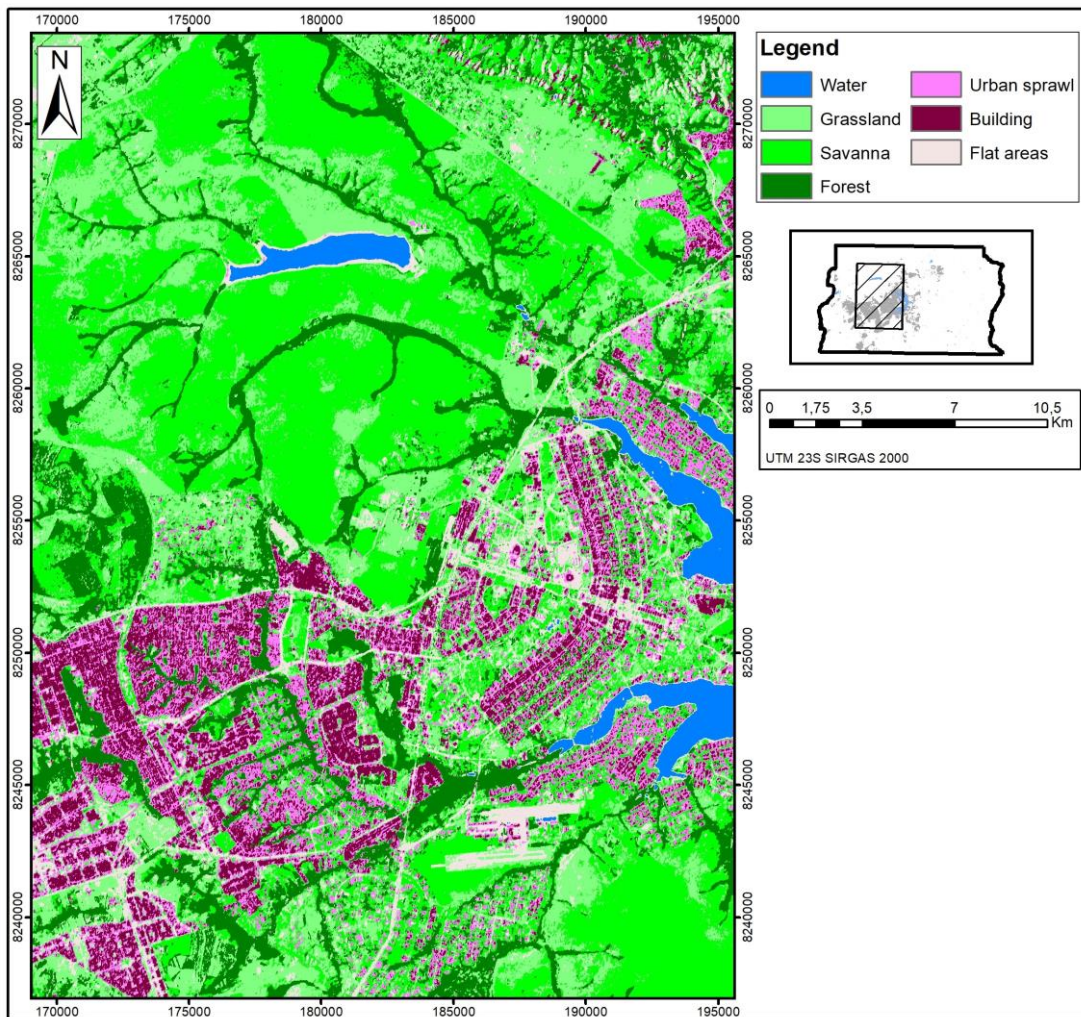
(a)



(b)

Org.: Authors, 2020

Figure 13. Final LULC map.



Org.: Authors, 2020

FINAL CONSIDERATIONS

This study innovates by presenting a methodological approach for LULC mapping based on intensities and interferometric coherence from a Sentinel 1 time series. The accuracy metrics indicate an improvement of 0.50 to 0.75 (Kappa) and 0.54 to 0.79 (F1-score) in the classifications with the interferometric coherence in time series, presenting a better balance between the accuracy and recall values.

This improvement is more evident in the vegetation classes, mainly in those with higher vegetative density (Forest), whose indexes varied from 0.47 to 0.93 (F1), which indicates the importance of this SAR information as a complementary approach to the improvement of the classification performance.

Furthermore, the results indicate that such insertion impairs classifiers' ability to identify

urban objects because coherence produces the smoothing of SAR metric values, which is not favourable to the classification of geometric targets because they have a high frequency. Thus, we determine this class using only metrics of intensity in both polarizations. Likewise, the compilation of methodologies for the LULC mapping identifies with greater precision both natural classes and the geometric definition of urban objects. Other studies can be developed to improve the classification process using object-oriented classifiers, a fusion of optical and radar sensors, and Deep Learning based on time cubes that consider temporal variation.

REFERENCES

AUBLANC, J.; MOREAU, T.; THIBAUT, P.; BOY, F.; RÉMY, F.; PICOT, N. Evaluation of SAR altimetry over the Antarctic ice sheet from

- CryoSat-2 acquisitions. **Advances in Space Research**, v. 62, n. 6, p. 1307-1323, 2018. <https://doi.org/10.1016/j.asr.2018.06.043>
- BELGIU, M.; DRAGUT, L. Random forest in remote sensing: A review of applications and future directions. **ISPRS Journal of Photogrammetry and Remote Sensing**, v. 114, p. 24-31, 2016. <https://doi.org/10.1016/j.isprsjprs.2016.01.011>
- BITENCOURT, M. D. **Classificação espectral-temporal da cultura de grãos em imagens Sentinel (SAR) utilizando Machine Learning em Luís Eduardo Magalhães, Brasil**. 2020. 39f. Thesis (Master Degree in Geography) – Universidade de Brasília, Brasília, 2020. <https://repositorio.unb.br/>
- BRASIL. Governo de Distrito Federal – GDF. **Zoneamento Ecológico-Econômico do Distrito Federal (ZEE/DF)**. Brasília, 2018. <http://www.zee.df.gov.br/>
- BRASIL. Instituto Brasileiro de Geografia e Estatística – IBGE. **Resolução n01/2015 que trata da transformação entre os referenciais geodésicos no Brasil**. Rio de Janeiro, 2015. ftp://geoftp.ibge.gov.br/metodos_e_outros_documentos_de_referencia/normas/rpr_01_2015_sirgas2000.pdf
- BREIMAN, L. Random Forests. **Machine Learning**, v. 45, n. 1, p. 5-32, 2001. <https://doi.org/10.1023/A:1010933404324>
- CAO, R.; TU, W.; YANG, C.; LI, Q.; LIU, J.; ZHU, J.; ZHANG, Q.; LI, Q.; QIU, G. Deep learning-based remote and social sensing data fusion for urban region function recognition. **ISPRS Journal of Photogrammetry and Remote Sensing**, v. 163, p. 82-97, 2020. <https://doi.org/10.1016/j.isprsjprs.2020.02.014>
- CHATURVEDI, S. K.; BANERJEE, S.; LELE, S. An assessment of oil spill detection using Sentinel 1 SAR-C images. **Journal of Ocean Engineering and Science**, in press, 2019. <https://doi.org/10.1016/j.joes.2019.09.004>
- CIAMPALINI, A.; SOLARI, L.; GIANNECCHINI, R.; GALANTI, Y.; MORETTI, S. Evaluation of subsidence induced by long-lasting building load using InSAR technique and geotechnical data: The case study of a Freight Terminal (Tuscany, Italy). **International Journal of Applied Earth Observation and Geoinformation**, v. 82, 2019. <https://doi.org/10.1016/j.jag.2019.101925>
- COSTA, D. H. **Uso de séries temporais Sentinel 1 na identificação de culturas agrícolas utilizando modelos de Machine Learning**. 2020. 51f. Thesis (Master Degree in Geography) – Universidade de Brasília, Brasília, 2020. <https://repositorio.unb.br/>
- DE ZAN, F.; GUARNIERI, A. M. TOPSAR: Terrain Observation by Progressive Scans. **IEEE Transactions on Geoscience and Remote Sensing**, v. 44, n. 9, p. 2352-2360, 2006. <https://doi.org/10.1109/TGRS.2006.873853>
- DINIZ, J. M. F. S.; GAMA, F. F. Utilização da coerência interferométrica SAR para mapeamento do uso e cobertura da terra na região da Amazônia. In: Simpósio Brasileiro de Sensoriamento Remoto, 2019, Santos/SP. **Anais...** São José dos Campos: INPE, 2019. Available in: <https://proceedings.science/sbsr-2019/papers/utilizacao-da-coerencia-interferometrica-sar-para-mapeamento-do-uso-e-cobertura-da-terra-na-regiao-da-amazonia>
- FERREIRA, G. H. S. **Identificação de áreas inundáveis na porção sul de Roraima com auxílio de imagens de radar**. 2018. 75f. Thesis (Master Degree in Geography) – Universidade de Brasília, Brasília, 2018. <https://repositorio.unb.br/handle/10482/33928>
- GRIFFITHS, P.; HOSTERT, P.; GRUEBNER, O.; LINDEN, V. Mapping megacity growth with multi-sensor data. **Remote Sensing of Environment**, v. 114, n. 2, p. 426-439, 2010. <https://doi.org/10.1016/j.rse.2009.09.012>
- HU, L.; DAI, K.; XING, C.; LI, Z.; TOMÁS, R.; CLARK, B.; SHI, X.; CHEN, M.; ZHANG, R.; QIU, Q.; LU, Y. Land subsidence in Beijing and its relationship with geological faults revealed by Sentinel 1 InSAR observations. **International Journal of Applied Earth Observation and Geoinformation**, v. 82, 2019. <https://doi.org/10.1016/j.jag.2019.05.019>
- KHALIL, R. Z.; HAQUE, S. InSAR coherence-based land cover classification of Okara, Pakistan. **The Egyptian Journal of Remote Sensing and Space Sciences**. v. 21, p. S23-S28, 2018. <https://doi.org/10.1016/j.ejrs.2017.08.005>
- LAWRENCE, R. L.; MORAN, C. J. The AmericaView Classification Methods Accuracy Project: A Rigorous Approach for Model Selection. **Remote Sensing of Environment**, v. 170, p. 115-120, 2015. <https://doi.org/10.1016/j.rse.2015.09.008>
- LI, M.; ZHANG, L.; DING, C.; LI, W.; LUO, H.; LIAO, M.; XU, Q. Retrieval of historical surface displacements of the Baige landslide from time-series SAR observations for retrospective analysis of the collapse event. **Remote Sensing of Environment**, v. 240, 2020. <https://doi.org/10.1016/j.rse.2020.111695>
- MARQUES, J. B.; CARVALHO JÚNIOR, O. A.; CAMPAGNOLI, F.; MESQUITA JÚNIOR, H. N.; GOMES, R. A. T.; GUIMARÃES, R. F. Classificação da cobertura da terra na região da ilha do Bananal usando imagens multitemporais PALSAR-2/ALOS-2. **Revista Franco-Brasileira de Geografia (Confins)**, v. 39, 2019. <https://doi.org/10.4000/confins.17506>
- MAXWELL, A. E.; WARNER, T. A.; FANG, F. Implementation of machine-learning classification in remote sensing: an applied review. **International Journal of Remote Sensing**, v. 39, n. 9, p. 2784-2817, 2018. <https://doi.org/10.1080/01431161.2018.1433343>
- MIGUEL, B. H.; SANO, E. E. Classificação do uso e cobertura da terra do Distrito Federal, Brasil a partir de dado de coerência interferométrica. **Revista Brasileira de Geografia Física**, v. 12, n. 2, p. 427-442, 2019. <https://doi.org/10.26848/rbgf.v12.2.p427-442>

- MOHAMMADIMANESH, F.; SALEHI, B.; MAHDIANPARI, M.; BRISCO, B.; MOTAGH, M. Multi-temporal, multi-frequency, and multipolarization coherence and SAR backscatter analysis of wetlands. *ISPRS Journal of Photogrammetry and Remote Sensing*, v. 142, p. 78-93, 2018. <https://doi.org/10.1016/j.isprsjprs.2018.05.009>
- OLESK, A.; PRAKS, J.; ANTROPOV, O.; ZALITE, K.; ARRUMAE, T.; VOORMANSIK, K. Interferometric SAR Coherence Models for Characterization of Hemiboreal Forests Using TanDEM-X Data. *Remote Sensing*, v. 8, n. 9, 2016. <https://doi.org/10.3390/rs8090700>
- OZIGIS, M. S.; KADUK, J. D.; JARVIS, C. H.; BISPO, P. C.; BALZTER, H. Detection of oil pollution impacts on vegetation using multifrequency SAR, multispectral images with fuzzy forest and random forest methods. *Environmental Pollution*, v. 256, 2020. <https://doi.org/10.1016/j.envpol.2019.113360>
- OLIVEIRA, P. D. S. **Uso de aprendizagem de máquina e redes neurais convolucionais profundas para a classificação de áreas queimadas em imagens de alta resolução espacial**. 2019. 34f. Thesis (Master Degree in Geography) – Universidade de Brasília, Brasília, 2019. <https://repositorio.unb.br>
- PICHIERRI, M.; HAJNSEK, I.; ZWIEBACK, S.; RABUS, B. On the potential of Polarimetric SAR Interferometry to characterize the biomass, moisture and structure of agricultural crops at L-, C- and X-Bands. *Remote Sensing of Environment*, v. 204, p. 596-616, 2018. <https://doi.org/10.1016/j.rse.2017.09.039>
- PRINZIE, A.; VAN DEN POEL, D. Random Forests for multiclass classification: Random MultiNomial Logit. *Expert systems with Applications: An International Journal*, v. 34, n. 3, p. 1721-1732, 2008. <https://doi.org/10.1016/j.eswa.2007.01.029>
- RAJAH, P.; ODINDI, J.; MUTANGA, O. Feature level image fusion of optical imagery and Synthetic Aperture Radar (SAR) for invasive alien plant species detection and mapping. *Remote Sensing Applications: Society and Environment*, v. 10, p. 198-208, 2018. <https://doi.org/10.1016/j.rsase.2018.04.007>
- SALGADO, C. B. **Emprego de séries temporais na Amazônia: análise de imagens MODIS e RADAR para mapeamento de uso e ocupação do solo no Estado do Acre**. 2019. 113f. Thesis (Doctorate Degree in Geography) – Universidade de Brasília, Brasília, 2019. <https://repositorio.unb.br/handle/10482/35999>
- SALGADO, C. B.; CARVALHO JÚNIOR, O. A.; GOMES, R. A. T.; GUIMARÃES, R. F. Análise da interferência de nuvens na classificação de séries temporais MODIS-NDVI na região da Amazônia, município de Capixaba, Acre. *Sociedade & Natureza*, v. 31, p. 1-20, 2019. <https://doi.org/10.14393/SN-v31-2019-47062>
- SEKERTEKIN, A.; MARANGOZ, A. M.; ADBIKAN, S. ALOS-2 and Sentinel-1 SAR data sensitivity analysis to surface soil moisture over bare and vegetated agricultural fields. *Computers and Electronics in Agriculture*, v. 171, 2020. <https://doi.org/10.1016/j.compag.2020.105303>
- SICA, F.; PULELLA, A.; NANNINI, M.; PINHEIRO, M.; RIZZOLI, P. Repeat-pass SAR interferometry for land cover classification: A methodology using Sentinel-1 Short-Time-Series. *Remote Sensing of Environment*, v. 232, 2019. <https://doi.org/10.1016/j.rse.2019.111277>
- WEGMULLER, U.; SANTORO, M.; WERNER, C.; CARTUS, O. On the estimation and interpretation of Sentinel 1 TOPS InSAR coherence. In: *Proc. of FRINGE 2015 Workshop*, Frascati, Italia, 23-27 março, ESA, 2015. <http://proceedings.esa.int/files/89.pdf>
- WERNER, A.; STORIE, C. D.; STORIE, J. Evaluating SAR-Optical Image Fusions for Urban LULC Classification in Vancouver Canada. *Canadian Journal of Remote Sensing*, v. 40, n. 4, p. 278-290, 2014. <https://doi.org/10.1080/07038992.2014.976700>
- WHITCOMB, J.; MOGHADDAM, M.; MCDONALD, K.; KELLNDORFER, J.; PODEST, E. Mapping vegetated wetlands of Alaska using L-band radar satellite imagery. *Canadian Journal of Remote Sensing*, v. 35, n. 1, p. 54-72, 2009. <https://doi.org/10.5589/m08-080>
- ZHANG, H.; LI, J.; WANG, T.; LIN, H.; ZHENG, Z.; LI, Y.; LU, Y. A manifold learning approach to urban land cover classification with optical and radar data. *Landscape and Urban Planning*, v. 172, p. 11-24, 2018. <https://doi.org/10.1016/j.landurbplan.2017.12.009>
- ZHU, Z.; ZHOU, Y.; SETO, K. C.; STOKES, E. C.; DENG, C.; PICKETT, S. T. A.; TAUBENBOCK, H. Understanding an urbanizing planet: Strategic directions for remote sensing. *Remote Sensing of Environment*, v. 228, p. 164-182, 2019. <https://doi.org/10.1016/j.rse.2019.04.020>

AUTHORS' CONTRIBUTION

Felipe Lima Ramos Barbosa and Renato Fontes Guimarães designed the study, analyzed the data and wrote the text. Felipe Lima Ramos Barbosa collected the data and processed the information and Renato Fontes Guimarães guided the progress of the work. Osmar Abílio de Carvalho Júnior and Roberto Arnaldo Trancoso Gomes evaluated the results and ensured the consistency of the data, as well as corrected the text produced.



This is an Open Access article distributed under the terms of the Creative Commons Attribution License, which permits unrestricted use, distribution, and reproduction in any medium, provided the original work is properly cited